Showcasing research from Professor Wan Jiang's laboratory, College of Materials Science and Engineering, Donghua University, Shanghai, China.

$Mg_3(Bi,Sb)_2$-based thermoelectric modules for efficient and reliable waste-heat utilization up to 750 K

This work presents the first thermoelectric module based on $Mg_3(Bi,Sb)_2$-based alloys with operating temperatures up to 750 K. An efficiency of 9.1% is achieved, exceeding that of state-of-the-art single-stage thermoelectric modules. Moreover, the module contains non-toxic elements and offers a higher power/cost ratio than existing modules, demonstrating the great feasibility for broad applications in mid-temperature waste heat recovery. The authors acknowledge Fantastic Color Co., Ltd. for making the cover image.

As featured in:

See Qihao Zhang, Lianjun Wang, Kornelius Nielsch *et al.*, *Energy Environ. Sci.*, 2022, **15**, 3265.

ROYAL SOCIETY OF CHEMISTRY

rsc.li/ees

Registered charity number: 207890

Energy & Environmental Science

ROYAL SOCIETY OF CHEMISTRY

PAPER

View Article Online
View Journal | View Issue

Cite this: *Energy Environ. Sci.*, 2022, **15**, 3265

$Mg_3(Bi,Sb)_2$-based thermoelectric modules for efficient and reliable waste-heat utilization up to 750 K†

Yuntian Fu, ‡[a] Qihao Zhang, ‡*[b] Zhongliang Hu,[a] Meng Jiang,[a] Aibin Huang,[c] Xin Ai,[b] Shun Wan,[d] Heiko Reith,[b] Lianjun Wang,*[a] Kornelius Nielsch*[be] and Wan Jiang[af]

Thermoelectric modules can directly convert the waste heat released by plants or vehicles into useful electricity, providing a clean and sustainable way to use fossil energy more efficiently. However, their commercial application in power generation, especially at temperatures above 500 K, has proceeded very slowly due to the low module efficiency, scarce or toxic constituent elements, and lack of stable metallization at high temperatures. Here, we develop a highly efficient, environmentally friendly and cost-effective thermoelectric module by using n-type Se-doped $Mg_3(Bi,Sb)_2$ and p-type $CoSb_3$-based skutterudite. The module can operate robustly up to 750 K and achieves a conversion efficiency of over 9% under a temperature difference of 450 K, superior to that of state-of-the-art single-stage thermoelectric modules. These achievements result from a comprehensive study involving optimization of the material composition and microstructure, screening for effective diffusion barrier layers, and rational design of the module structure. Our work demonstrates the feasibility and scalability of efficient and reliable thermoelectric modules based on sustainable elements for broad applications in mid-temperature waste heat recovery.

Received 30th March 2022,
Accepted 13th June 2022

DOI: 10.1039/d2ee01038k

rsc.li/ees

Introduction

The worldwide energy crisis caused by the increasing use of fossil fuels due to enhanced energy consumption and thereby the production of very large amounts of greenhouse gases such as CO_2 is one of the most severe problems faced by human beings. Excess heat, as a byproduct of combustion and industrial processes, is a ubiquitous unutilized energy resource that is still primarily considered waste. Effective harnessing of this heat energy would enable significant improvements in the energy efficiency of fossil fuel utilization and thereby mitigation of CO_2 emissions. There have been various innovative attempts to harness waste heat to convert it into usable forms of energy, such as electricity. Among them, thermoelectric (TE) modules based on the Seebeck effect stand out owing to their advantages of solid-state operation without moving parts, virtually maintenance-free nature, and compactness for integration into existing systems.[1,2] A TE module is commonly made up of a number of n- and p-type TE legs that are connected electrically in series and thermally in parallel. The theoretical maximum efficiency (η_{max}) of a TE module depends on the average zT (zT_{ave}) of TE materials over a wide temperature range as well as the temperature difference between the hot (T_h) and cold (T_c) sides of the module as follows:

$$\eta_{max} = \frac{T_h - T_c}{T_h} \cdot \frac{\sqrt{1 + zT_{ave}} - 1}{\sqrt{1 + zT_{ave}} + \frac{T_c}{T_h}} \quad (1)$$

Over the past decades, research into TE materials has substantially grown. A variety of approaches, including electronic band engineering,[3,4] design of multiscale hierarchical architectures,[5] and entropy engineering,[6] have succeeded in

[a] *State Key Laboratory for Modification of Chemical Fibers and Polymer Materials & College of Materials Science and Engineering, Donghua University, Shanghai, 201620, China. E-mail: wanglj@dhu.edu.cn*
[b] *Institute for Metallic Materials, Leibniz Institute for Solid State and Materials Research Dresden (IFW Dresden), Dresden, 01069, Germany. E-mail: k.nielsch@ifw-dresden.de, q.zhang@ifw-dresden.de*
[c] *State Key Laboratory of High Performance Ceramics and Superfine Microstructure, Shanghai Institute of Ceramics, Chinese Academy of Sciences, Shanghai, 200050, China*
[d] *Center for High Pressure Science and Technology Advanced Research (HPSTAR), Shanghai, 201203, China*
[e] *Institute of Materials Science, Dresden University of Technology, Dresden, 01062, Germany*
[f] *Institute of Functional Materials, Donghua University, Shanghai, 201620, China*
† Electronic supplementary information (ESI) available. See DOI: https://doi.org/10.1039/d2ee01038k
‡ These authors contributed equally to this work.

pushing zT_{ave} above 1.0. These remarkable advances are widely considered sufficient to enable next-generation TE modules with efficiencies exceeding the previous values by more than a factor of two.[1] However, the development of corresponding TE modules has proceeded quite slowly. Currently, commercially available TE modules for power generation are mainly Bi_2Te_3-based modules.[7,8] The optimal operating temperature of these modules is still below 500 K due to the unfavorable bipolar effect induced by the narrow bandgap of Bi_2Te_3,[8] and they are limited to niche applications due to the low conversion efficiency (approximately 5–6%)[9,10] and scarcity of elemental Te.[9]

In practice, recovery of waste heat up to the mid-temperature range (500–800 K),[11] which matches the majority of industrial waste heat sources suitable for energy harvesting,[12] offers greater application potential and is thus the area for which TE materials have been most intensively developed, such as PbTe,[3,5] GeTe,[11,13] SnSe,[4,14] skutterudite (SKD),[15] Cu_2Se,[16] and half-Heusler (HH).[17] Among them, TE modules based on PbTe-related alloys are the most developed and have demonstrated successful use as radioisotope TE generators in several space missions.[1,18] However, their large-scale industrial application is impeded by the toxicity of Pb and the scarcity of Te. The development of TE modules using other materials is also plagued by different challenges, such as the high cost of GeTe,[19] the extreme oxygen sensitivity in the synthesis of SnSe,[14] and the instability of Cu_2Se due to electromigration of Cu ions.[16] Therefore, strong desire for next-generation mid-temperature TE modules warrants the development of high-efficiency, cost-effective and stable alternatives.

In recent years, $Mg_3(Bi,Sb)_2$ alloys have shown exceptional TE properties from 300 K to 750 K and are regarded as one of the most promising materials for large-scale applications in the future because of their nontoxic nature, abundant constituent elements, and excellent mechanical robustness.[20–24] Several groups have thereby embarked on module development and have recently demonstrated remarkable outcomes.[8–10] Nevertheless, most of these research activities target modules that operate below 600 K, aiming to replace traditional Bi_2Te_3 alloys. Despite the advances, these studies still fall far from achieving the optimum application potential of $Mg_3(Bi,Sb)_2$ alloys. The goal of using $Mg_3(Bi,Sb)_2$-based TE modules for power generation above 600 K has not yet been realized, as issues related to material design, contact optimization, module assembly and service reliability are more challenging at higher temperatures.

Herein, through full exploitation from material modification to module engineering, we demonstrate for the first time high-efficiency and cost-effective $Mg_3(Bi,Sb)_2$-based TE modules for waste heat utilization up to 750 K (Fig. 1). To achieve this, we first tailored the band structure and microstructure of the Mg_3Bi_2–Mg_3Sb_2 compounds, and thus realized a $zT_{ave} > 1$ from 300 to 700 K in $Mg_{3.2}Bi_{0.996}SbSe_{0.004}$. Then, by developing a novel high-throughput screening method, we identified Nb as a suitable barrier material that enables a low interfacial contact resistivity (ρ_c of 9.7 μΩ cm^2) and exceptional interfacial stability (ρ_c of 26 μΩ cm^2 after accelerated thermal ageing at 773 K for 360 h). In addition, we investigated the compatibility of currently available p-type TE materials that feature high performance and environmentally friendliness with the Mg_3Bi_2–Mg_3Sb_2 compounds and employed finite element simulations to design the geometrical configuration of the TE modules. All these efforts resulted in a module consisting of n-type $Mg_{3.2}Bi_{0.996}SbSe_{0.004}$ and p-type $Ce_{0.9}Fe_3CoSb_{12}$ with a high conversion efficiency of 9.1% at a heat source temperature (T_{heater}) of 748 K, surpassing that of state-of-the-art single-stage TE modules under the same temperature gradient (Fig. 1a). Moreover, our module does not contain toxic elements and offers a higher power/cost ratio than existing modules (Fig. 1b, and Supplementary note, ESI,†), *e.g.*, two orders of magnitude more cost effective than GeTe-based modules, which spurs prospects for large-scale commercial applications.

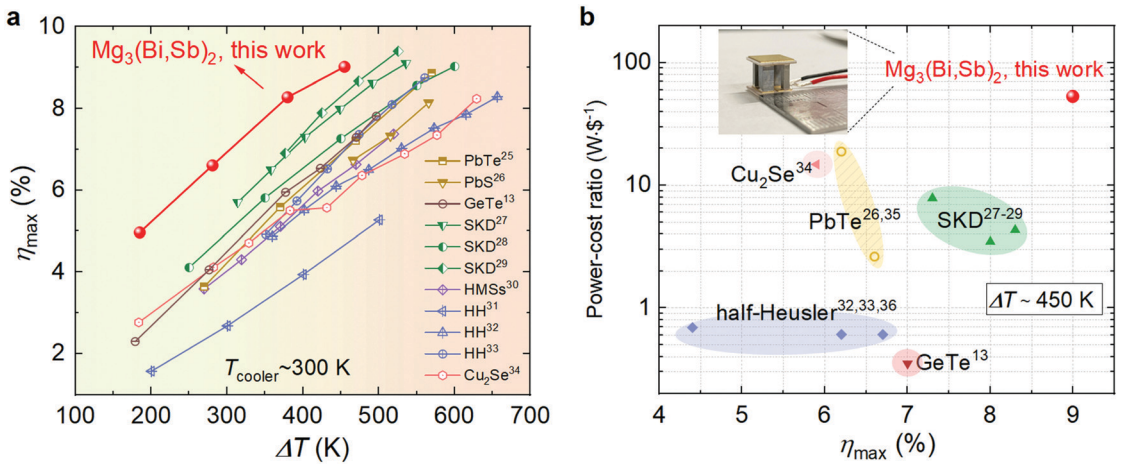

Fig. 1 Performance of our $Mg_3(Bi,Sb)_2$-based TE module in comparison to other mid-temperature counterparts. (a) Maximum conversion efficiency (η_{max}) as a function of temperature difference (ΔT) for the $Mg_{3.2}Bi_{0.996}SbSe_{0.004}$/$Ce_{0.9}Fe_3CoSb_{12}$ module. Literature results of the state-of-the-art TE modules are included for comparison.[13,25–34] (b) Comparisons of the cost effectiveness and η_{max} of different TE modules under a ΔT of 450 K (PbTe,[26,35] GeTe,[13] SKD,[27–29] HH,[32,33,36] Cu_2Se[34]). The cost of TE materials is used for the comparison, which is calculated by using the element prices from IYPT 2019.[37] The inset shows a photograph of our module.

Results and discussion

TE properties of Se-doped $Mg_{3.2}Bi_{2-x}Sb_x$

Mg_3Bi_2 is a semimetal, and Mg_3Sb_2 is a semiconductor;[22] and it has been reported that alloying Mg_3Bi_2 with Mg_3Sb_2 can enhance the bandgap and suppress the bipolar contribution of Bi-rich compositions, pushing the maximum zT (zT_{max}) to higher temperatures.[22] However, to obtain satisfactory zT_{ave} towards mid-temperature power generation applications, further optimization on the carrier concentration and modulation of electron–phonon interaction are necessary. Herein, we synthesized a series of samples with the nominal composition of $Mg_{3.2}Bi_{2-x-y}Sb_xSe_y$ (x = 0.3, 0.5, 1, 1.5, 1.7, y = 0.004, 0.008, 0.012). Given the scarcity of Te, Se is used as the anionic dopant to optimize the carrier concentration with the aim of achieving cost-effective TE materials for large-scale applications. In addition, recent reports suggest that Se can substitute Te as an effective n-type dopant in Mg_3Sb_2-based materials,[38–41] which underlines their possible application for next-generation mid-temperature TE modules with earth-abundant and inexpensive component elements.

Small samples in a typical dimension – a disk with a diameter of 10 mm and a thickness of 2 mm – were first prepared for structural and performance analysis. Powder X-ray diffraction (XRD) patterns (Fig. S1, ESI†) and energy dispersive spectroscopy (EDS) analyses (Fig. S2, ESI†) verify the single phase of all samples. Temperature-dependent electronic and thermal transport properties of small-sized $Mg_{3.2}Bi_{1.996-x}Sb_xSe_{0.004}$ samples are shown in Fig. S3 (ESI†), along with a detailed discussion. As a result, zT_{max} of approximately 1.3 is obtained for both $Mg_{3.2}Bi_{0.996}SbSe_{0.004}$ and $Mg_{3.2}Bi_{0.496}Sb_{1.5}Se_{0.004}$ samples (Fig. 2a). The zT_{ave} values from 300 to 700 K are calculated, and the maximum zT_{ave} exceeds 1.0 for the $Mg_{3.2}Bi_{0.996}SbSe_{0.004}$ sample, which is superior to that of most Se-doped Mg_3Bi_2–Mg_3Sb_2 alloys and is comparable to the high value recently reported by Mo *et al.*[41] (Fig. 2b). The high zT_{ave} of our $Mg_{3.2}Bi_{0.996}SbSe_{0.004}$ sample is mainly attributed to the high electrical conductivity due to the large grain size (Fig. S4, ESI†) achieved by using a high sintering temperature (Table S2, ESI†) without compromising the low thermal conductivity. This agrees with earlier reports. For example, Kanno *et al.* considerably enhanced the room temperature zT values of coarse-grained $Mg_{3.2}Sb_{1.5}Bi_{0.49}Te_{0.01}$ samples by increasing the sintering temperature from 873 K to 1123 K.[42] Larger grains lead to the reduction of detrimental grain boundary scattering,[42,43] resulting in higher carrier mobility. Furthermore, Pan *et al.* also found that the lattice thermal

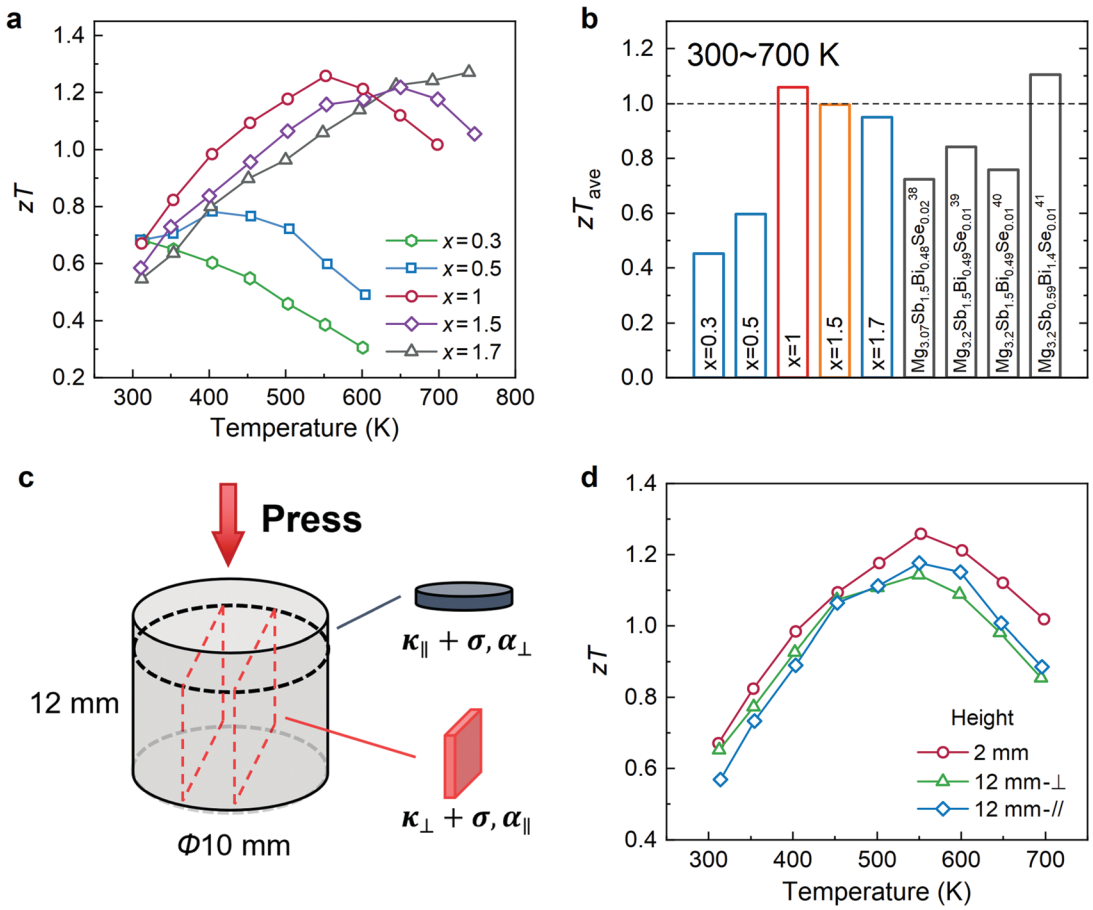

Fig. 2 TE transport properties of n-type $Mg_{3.2}Bi_{1.996-x}Sb_xSe_{0.004}$. (a) Temperature dependence of zT. (b) zT_{ave} of $Mg_{3.2}Bi_{1.996-x}Sb_xSe_{0.004}$ in this work compared with those of reported Se-doped $Mg_3(Bi,Sb)_2$ alloys.[38–41] (c) Schematic slicing diagram of the large-sized cylinders, showing the directions that TE transport properties were measured. (d) Comparison of the TE properties of large- and small-sized samples.

conductivity of n-type $Mg_3(Bi,Sb)_2$ polycrystalline samples is nearly independent of grain size, whereas electron mobility exhibits a significant increase with larger grain size.[24]

In addition, we also investigated the effect of different Se doping (y = 0.004, 0.008, 0.012) on the TE properties of x = 1.0 samples and found that the simultaneous increases in the power factor and thermal conductivity result in almost unchanged zT_{ave} values (Fig. S8, ESI†). Similar results can be also observed in the recent work of Mo *et al.*[41] This implies that slight fluctuations in the elemental content of Se do not seriously deteriorate the TE properties of $Mg_{3.2}Bi_{0.996}SbSe_{0.004}$, which ensures excellent reproducibility of the material during batch preparation and thus facilitates the fabrication of TE modules. More critically, considering that TE modules usually utilize the TE properties of sintered samples along the pressing direction, we further prepared large-sized cylinders to confirm the consistency of their properties (Fig. 2c). As a result, the electronic and thermal transport properties of the large- and small-sized samples are comparable (Fig. 2d and Fig. S9, ESI†), and each property is substantially isotropic. zT_{ave} of 1.0 is maintained for the large-sized samples (Fig. S9e, ESI†), enabling the development of high-performance TE modules.

Diffusion barrier material screening

In a TE module, p- and n-type TE materials are usually connected by electrodes to realize electric connection in series. During practical operation, the hot-side temperature usually reaches hundreds of degrees. As a result, commonly used electrode materials, such as Ni and Cu, can undergo severe chemical reactions and/or atomic diffusion with TE materials,[47] leading to degradation and instability of the module. Therefore, searching for a suitable diffusion barrier material that is almost chemically inert to TE materials, but offers low electrical contact resistivity (ρ_c) and good mechanical bonding, is an urgent task for any kind of TE material for mid-temperature applications.

Currently, Fe, Ni, 304 stainless steel and Mg_2Cu have been investigated as diffusion barrier materials for Mg_3Bi_2–Mg_3Sb_2 alloys.[8–10,44,45] Despite some advances, studies on interfacial stability are scarce and have mainly focused on temperatures below 600 K. The $Mg_{3.2}Sb_{1.5}Bi_{0.49}Te_{0.01}$/304 stainless steel junction exhibited a quite low initial ρ_c of 5.6 μΩ cm^2.[44,46] However,

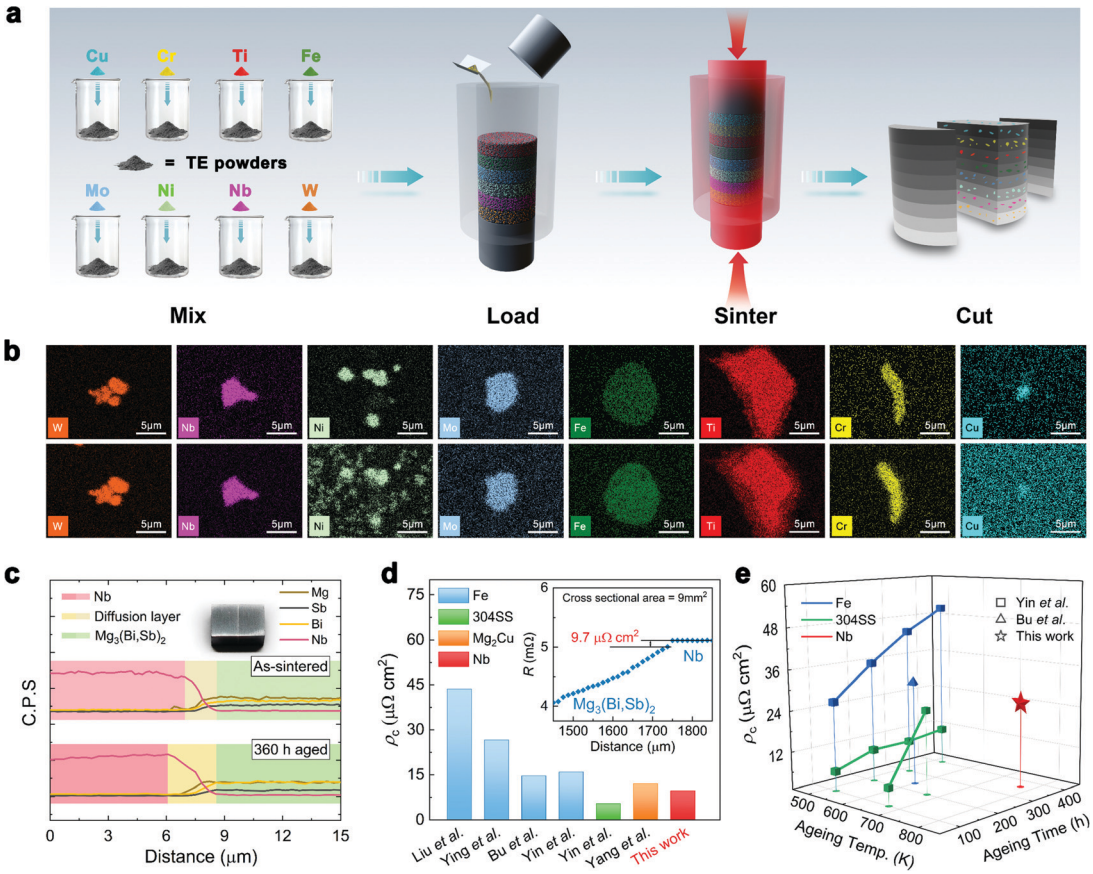

Fig. 3 Barrier layer design and interfacial stability. (a) Schematic diagram for high-throughput screening of the diffusion barrier layer for $Mg_{3.2}Bi_{0.996}SbSe_{0.004}$. (b) EDS mapping results showing the elemental distribution of different barrier layer candidates within the $Mg_{3.2}Bi_{0.996}SbSe_{0.004}$ matrix before and after thermal ageing at 773 K for 360 h in vacuum. (c) EDS line scanning results of the $Mg_{3.2}Bi_{0.996}SbSe_{0.004}$/Nb junction before and after ageing. The inset is a photo of the tested sample. (d) Measured contact resistivity (ρ_c) of the as-sintered $Mg_{3.2}Bi_{0.996}SbSe_{0.004}$/Nb junction in comparison with literature results.[8–10,44,45] The inset shows a typical resistance scanning result. (e) ρ_c of the $Mg_{3.2}Bi_{0.996}SbSe_{0.004}$/Nb junction as a function of thermal ageing temperature and time. Data from the literature are included for comparison.[8,44,46]

it significantly increased to 25 μΩ cm^2 after thermal ageing under 673 K for 200 h.[46] The stability of the interface is unsatisfactory. Furthermore, previous attempts to identify barrier materials are based on a trial-and-error approach,[48] which is both time-consuming and less than ideal for finding the optimal combination. Recently, Xing *et al.* developed a high-throughput strategy to identify viable diffusion barrier layers for GeTe.[13] This approach is productive but still suffers from shortcomings, such as deactivation of candidate powders due to the inter-reaction or diffusion between themselves, and random dispersion of candidate powders making tracking the specific interfaces after thermal ageing difficult.

Herein, we develop a modified process for rapid and efficient screening of the diffusion barrier layer (Fig. 3a). First, the powders of different barrier layer candidates were separately mixed with TE powders at the same ratio. All mixtures were then loaded layer by layer into a graphite die and consolidated into a bulk sample by one-step sintering. Finally, segmented samples were obtained by cutting the sintered bulk along the direction of the sintering pressure and then used for characterization and thermal ageing. As a case study, we selected eight kinds of elemental powders (W, Nb, Ni, Mo, Fe, Ti, Cr, Cu) and mixed them with $Mg_{3.2}Bi_{0.996}SbSe_{0.004}$ powders at 1 vol%. Sintering was conducted by spark plasma sintering (SPS) technique following the sintering parameters for $Mg_{3.2}Bi_{0.996}SbSe_{0.004}$. Accelerated thermal ageing tests were carried out at 773 K for 360 h to identify the elemental reaction or diffusion in a shorter time. More details can be found in the Methods section.

Benefiting from the new approach, we can accurately track the changes in specific elements at specific locations after thermal ageing (Fig. 3b, Fig. S10 and S11, ESI†). As Fig. 3b shows, the microstructures of typical interfaces between $Mg_{3.2}Bi_{0.996}SbSe_{0.004}$ and different metals can be divided into three categories. The first category includes W. There is no obvious reaction or diffusion between the W particles and the $Mg_{3.2}Bi_{0.996}SbSe_{0.004}$ matrix before and after thermal ageing, indicating that W fails to form effective bonds with the matrix. The second category includes Ni, Cu, and Ti. All of them can form intimate contact with the surrounding $Mg_{3.2}Bi_{0.996}SbSe_{0.004}$ matrix by forming a reaction layer during the sintering process. However, the reaction is so violent that the metal particles are severely eroded away after thermal ageing, and therefore, these materials cannot satisfy the requirement of long-term operation at high temperatures. The third category includes Fe, Mo, Cr, and Nb. They all bond well to the matrix after sintering but do not generate visible reaction layers. After thermal ageing, reaction layers can be found in the vicinity of Fe particles (Fig. 3b and Fig. S11a, ESI†), but this is not the case with the other three particles. However, Mo particles shrink (Fig. 3b and Fig. S11b, ESI†) while Cr particles swell (Fig. 3b and Fig. S11c, ESI†) due to thermal ageing. Only Nb particles barely have any change (Fig. 3b and Fig. S11d, ESI†), suggesting that Nb is more appropriate as the diffusion barrier material for Mg_3Bi_2–Mg_3Sb_2 alloys in mid-temperature applications.

After confirming the chemical inertness of the barrier layer candidates through rapid screening, we further selected Nb to investigate the interfacial contact resistance. Nb foil was sintered with $Mg_{3.2}Bi_{0.996}SbSe_{0.004}$ to form sandwich-structured legs (inset of Fig. 3c), which were then used for accelerated thermal ageing experiments and characterization of the interfaces. There is a thin interfacial reaction layer of less than 2 μm at the as-sintered $Mg_{3.2}Bi_{0.996}SbSe_{0.004}$/Nb interface (Fig. 3c), resulting in a low contact resistivity (ρ_c) of ~9.7 μΩ cm^2 (Fig. 3d). The actual ρ_c value should be lower because the minimum probe step is 12.5 μm in this work due to the limitations of the measurement instrument, which is much larger than the thickness of the interfacial reaction layer shown in Fig. 3c. Despite this, this value is still lower than most of the reported data (Fig. 3d). More critically, even after accelerated thermal ageing at 773 K for 360 h, the interfacial reaction layer remains thin at less than 3 μm (Fig. 3c), yielding a ρ_c as low as 26 μΩ cm^2 (Fig. 3e).

This is the first study of the long-term service performance of a $Mg_3(Bi,Sb)_2$-based TE junction at temperatures as high as 773 K (Fig. 3e), and the junction shows exceptional interfacial stability. This superiority may be attributed to the combination of a low interfacial bonding energy and a large activation energy barrier for elemental migration between Nb and $Mg_{3.2}Bi_{0.996}SbSe_{0.004}$,[29] which facilitates the application of $Mg_3(Bi,Sb)_2$-based TE modules at elevated temperatures. Moreover, despite the difference in the coefficient of thermal expansion (CTE) between the Nb and Mg_3Bi_2–Mg_3Sb_2 alloys, no cracks are observed near the interface areas (Fig. S12, ESI†) due to the use of thin Nb foil (thickness of 30 μm, see Methods).

P-type material selection and module geometry design

To fabricate mid-temperature TE modules for large-scale applications, p-type high-performance TE materials consisting of abundant and nontoxic elements are also necessary. In this regard, we selected ten state-of-the-art p-type Pb&Te-free TE materials from previous reports[14,27,36,49–55] and predicted the power generation performance of the modules constructed using them along with n-type $Mg_{3.2}Bi_{0.996}SbSe_{0.004}$ (Fig. 4a and b). Finite element simulations were employed to obtain the optimal geometrical configuration, especially the cross-sectional area ratio of the p- and n-legs (A_p/A_n), for the maximum conversion efficiency (η_{max}). We can see that at temperatures of 700 K and 300 K for the hot-side (T_h) and cold-side (T_c) ceramic plates, respectively, an η_{max} of over 10% can be achieved by combining a variety of p-type materials with $Mg_{3.2}Bi_{0.996}SbSe_{0.004}$ (Fig. 4b), such as ZrCoBi, $CoSb_3$, Zn_4Sb_3, Cu_2Se, SnSe, BiCuSeO, and $CaMg_2Bi_2$. This is motivating, as we have a wider choice of materials. However, in terms of developing practical modules, there are some challenging issues, such as the anisotropic TE properties of SnSe and BiCuSeO, phase transition and elemental migration in Zn_4Sb_3 and Cu_2Se, that block full development. In this regard, $Ce_{0.9}Fe_3CoSb_{12}$ is preferred because it offers good stability up to 750 K,[29] isotropic characteristics and, more importantly, well-established production.[27,56]

After determining an appropriate p-type TE material, we further optimized the ratio of the height and cross-sectional area (H/A_{pn}) for optimal power generation performance. A_p/A_n is set to 1/3 based on the above results. Clearly, η_{max} and the maximum power density ($P_{d,max}$) show opposite trends as a

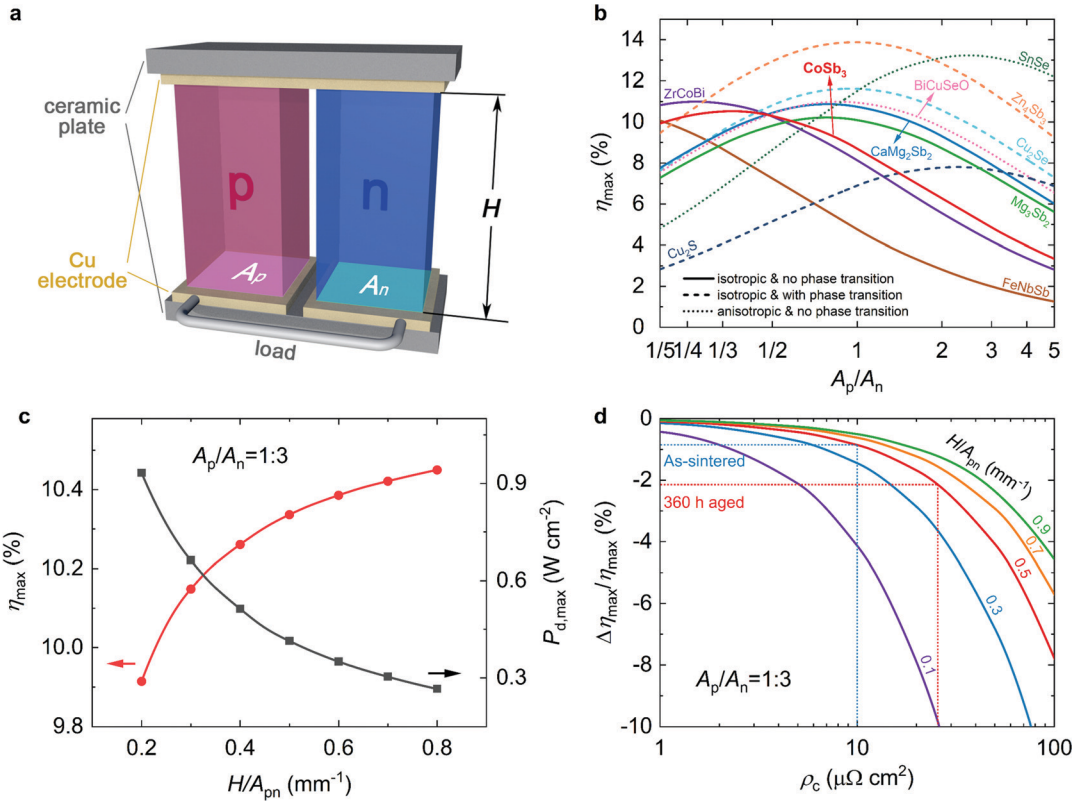

Fig. 4 Multiparameter design of $Mg_3(Bi,Sb)_2$-based TE modules. (a) Geometrical model for finite element simulation. (b) Matching design of n-type $Mg_{3.2}Bi_{0.996}SbSe_{0.004}$ with ten different p-type TE candidates to maximize the maximum conversion efficiency (η_{max}). A_p/A_n represents the cross-sectional area ratio of p- and n-legs. The heat boundary conditions are set to T_h = 700 K and T_c = 300 K, where T_h and T_c represent the temperatures of the hot-side and cold-side ceramic plates, respectively. The ratio of the height and cross-sectional area (H/A_{pn}) is fixed to 0.3 mm^{-1}. (c) Simulated η_{max} and maximum power density ($P_{d,max}$) as a function of H/A_{pn} for the $Mg_{3.2}Bi_{0.996}SbSe_{0.004}/Ce_{0.9}Fe_3CoSb_{12}$ TE module. (d) Effect of interface contact resistivity on the efficiency loss of the $Mg_{3.2}Bi_{0.996}SbSe_{0.004}/Ce_{0.9}Fe_3CoSb_{12}$ module.

function of H/A_{pn} (Fig. 4c). This is because the effective temperature difference across the TE legs is enlarged by increasing the leg height, which leads to an increase in η_{max}.[56] However, the module resistance is also enlarged, resulting in a decrease in $P_{d,max}$. We can also notice that η_{max} increases more and more slowly and tend to stabilize with the increase of H/A_{pn}, while $P_{d,max}$ significantly decreases with increasing H/A_{pn} (Fig. 4c). For example, when H/A_{pn} is increased from 0.2 to 0.8 mm^{-1}, the η_{max} increases by ~5%, while the corresponding $P_{d,max}$ decreases by ~70%. Therefore, H/A_{pn} should be determined by balancing the η_{max} and $P_{d,max}$ requirements for practical applications.

In addition, the determination of H/A_{pn} is closely related to the interface contact resistance. This is because a higher ρ_c leads to higher losses in the conversion efficiency, and the losses increase when H/A_{pn} decreases (Fig. 4d). As discussed above, the ρ_c for the $Mg_{3.2}Bi_{0.996}SbSe_{0.004}$/Nb interface in this work is 9.7 and 26 μΩ cm^2 before and after thermal ageing, respectively. Therefore, taking these conflicting factors into account, we chose H/A_{pn} = 0.5 mm^{-1} to fabricate the TE modules considering that the corresponding efficiency loss is below 3% (Fig. 4d).

Module fabrication and performance evaluation

Based on the above achievements in optimization of TE materials and module engineering, we fabricated TE modules by using n-type $Mg_{3.2}Bi_{0.996}SbSe_{0.004}$ and p-type $Ce_{0.9}Fe_3CoSb_{12}$ (Fig. 5a, Fig. S13, ESI,† and Methods). The current (I), output voltage (V), output power (P), and TE conversion efficiency were measured under different ΔT with a T_{heater} of up to 748 K (see Methods). Circulating water with a fixed temperature of 288 K was used to cool the cold side. $\Delta T = T_{heater} - T_{cooler}$ in this work, where T_{cooler} is the temperature of the cold-side Cu block (Fig. S14, ESI†). Note that thermal resistances between the TE module and external heat/cold sources are inevitable due to imperfect contacts, leading to an additional temperature drop, and therefore, the effective temperature difference across the TE module is lower than ΔT. According to our previous calibration experiments,[56] when T_{heater} reaches 748 K, T_h is probably ~20 K lower than T_{heater}, and T_c may be ~10 K higher than T_{cooler}.

Tests reveal that each V–I curve exhibits a good linear relationship (Fig. 5b), where the slope indicates internal resistance (R_{in}) of the module at different ΔT, and the y-intercept represents the corresponding open-circuit voltage (V_{oc}). The maximum power output (P_{max}) is reached when the external load resistance is equal to R_{in}. The conversion efficiency at each current is calculated by using the output power and cold-side heat flow through eqn (2). As shown in Fig. 5c, the measured η_{max} increases with increasing T_{heater}, exceeding 9% at a T_{heater}

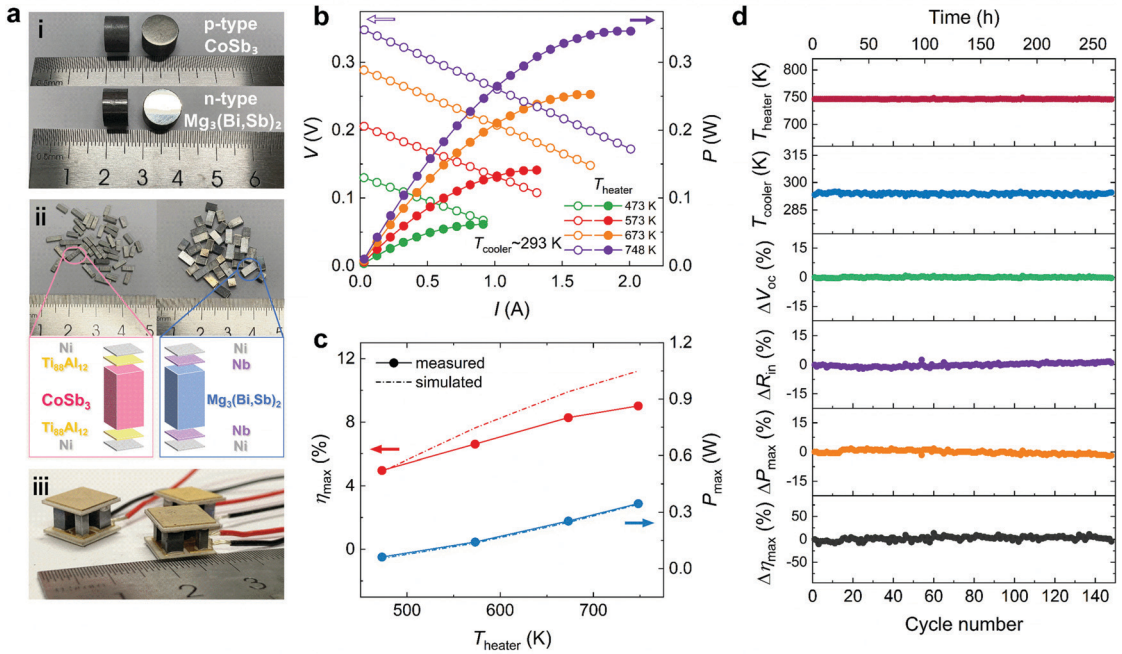

Fig. 5 Power generation performance of $Mg_3(Bi,Sb)_2$-based TE modules. (a) Schematic diagram illustrating the TE module fabrication flow. (b) Measured voltage (V) and output power (P) as a function of current (I) at different temperatures. Note that T_{heater} is the temperature of the heater, and T_{cooler} is the temperature of the cold-side Cu block. (c) Comparison of the measured η_{max} and maximum output power (P_{max}) with the corresponding simulated results. (d) Thermal cycling test results. From top to bottom, the results correspond to the temperature of the heater, the temperature of cold-side Cu block, the change of open-circuit voltage (V_{oc}), module resistance (R_{in}), maximum power output, and efficiency, respectively.

of 748 K with a corresponding ΔT of 455 K. We noticed that an efficiency of 9% was recently reported by Yin *et al.*,[44] which is quite impressive and inspiring, but it was achieved on a single n-type $Mg_{3.2}Sb_{1.5}Bi_{0.49}Te_{0.01}$ leg. The single-leg efficiency is very useful for assessing the potential of a single TE material, but is still far from real applications. Towards industrial applications, modules consisting of both n-type and p-type TE materials need to be developed. To the best of our knowledge, this is the first $Mg_3(Bi,Sb)_2$-based TE module that can operate at temperatures up to 750 K (Fig. S15, ESI†). More critically, the η_{max} of our module is higher than that of the state-of-the-art single-stage TE modules under the same temperature gradient (Fig. 1a and Fig. S16, ESI†). In addition, higher η_{max} is predicted, which could be achieved by optimizing the filling factor of our module and reducing the heat leakage from the gaps between TE legs.[9,26]

Furthermore, we conducted thermal cycling experiments to examine the long-term reliability of the module. During the measurements, T_{cooler} was maintained at ~293 K while T_{heater} was set to cycle between 473 K and 750 K (Fig. 5d). One cycle lasted approximately 110 min, and the module power generation performance was evaluated whenever T_{heater} was stabilized at 750 K. Measurements were carried out in a chamber filled with argon at an initial pressure of ~200 Pa. After 150 cycles (~275 h), V_{oc} remains stable (Fig. 5d). We did not observe an abrupt increment in R_{in} as reported in other mid-temperature TE modules,[13] indicating a much better module reliability. Both P_{max} and η_{max} are comparable to those before thermal cycling, showing a slight decrease of <5%. This demonstrates the great feasibility of $Mg_3(Bi,Sb)_2$-based TE modules for mid-temperature applications owing to their record-high conversion efficiency and excellent service stability.

Conclusions

TE modules can harvest waste heat and directly convert it to electricity, thereby improving fuel efficiency and mitigating CO_2 emissions. The tremendous advances in high-performance TE materials achieved over the past decades have raised expectations regarding the use of TE generators in various energy saving and energy management applications. However, the commercialization of TE generators, particularly those that can operate above 500 K, proceeds slowly due to the low conversion efficiency, high costs, toxicity of the constituent elements, and limited long-term service stability. We have therefore developed a novel high-performance TE module in this work by using the environmentally friendly and low-cost TE materials of n-type Se-doped $Mg_3(Bi,Sb)_2$ and p-type $CoSb_3$-based SKD. The module exhibits exceptional characteristics, including a high operating temperature of up to ~750 K, a record-high conversion efficiency of 9.1% under a temperature difference of ~450 K, a higher efficiency/price ratio than that of state-of-the-art TE modules, excellent interfacial stability, and good module reliability during thermal cycling. These achievements result from the full exploration involving tailoring of the material composition and microstructure, high-throughput screening of effective diffusion barrier layers, and optimization of the module structure. Our study has opened the door to the development of $Mg_3(Bi,Sb)_2$-based TE

modules for mid-temperature waste heat recovery. We believe that higher zT_{ave} values could be achieved by further optimization, such as by further doping at the cation site of $Mg_3(Bi,Sb)_2$, which will soon lead to module efficiency exceeding 10%. In this regard, our findings here bridge the gap between material discovery and module development, providing a viable route to accelerate subsequent research on fabricating efficient and stable TE modules.

Experimental

Material synthesis

High-purity elements of Bi (99.999%, Sinopharm Chemical Reagent Ltd), Sb (99.99%, Sinopharm Chemical Reagent Co.), Se (99%, Sinopharm Chemical Reagent Ltd), and Mg (99.9%, Sinopharm Chemical Reagent Ltd) were weighed according to the composition of $Mg_{3.2}Bi_{2-x-y}Sb_xSe_y$ (x = 0.3, 0.5, 1, 1.5, 1.7, y = 0.004, 0.008, 0.012). An excess Mg of 0.2 was chose based on previous studies (Table S1, ESI†). All the elements in total of 8 g were weighed at once and then loaded into a stainless-steel ball milling jar in a glove box under an argon atmosphere with oxygen and water levels below 0.1 ppm. The mixture was ball milled for 15 h at 550 rpm using a planetary mill machine (RETSCH PM100). Next, the ball-milled powders were loaded into a graphite die with an inner diameter of 10 mm. SPS (Dr Sinter: 2000) was then carried out to obtain dense bulk samples under a uniaxial pressure of 50 MPa at different temperatures (973–1073 K, Table S2, ESI†) for 3 min. The p-type $Ce_{0.9}Fe_3CoSb_{12}$ samples were synthesized following our previous work,[27] and the corresponding TE properties are shown in Fig. S17 (ESI†).

In the diffusion barrier screening experiments, high purity powders of W (99.95%, Adamas), Nb (99.99%, Alfa Aesar, 325 mesh), Ni (99.99% Macklin, 200 mesh), Mo (99.9%, Alfa Aesar, 100 mesh), Fe (99.99%, Adamas), Ti (99.99%, Macklin, 300 mesh), Cr (99.94%, Alfa Aesar, 200 mesh), and Cu (99.5%, Alfa Aesar, 150 mesh) were separately mixed with $Mg_{3.2}Bi_{0.996}SbSe_{0.004}$ powder at 1 vol%. The eight mixed powders were then sequentially added to a graphite die and sintered into a bulk by using the SPS technique following the above sintering parameters for $Mg_{3.2}Bi_{0.996}SbSe_{0.004}$.

TE module fabrication

n-Type TE joints of Ni/Nb/$Mg_{3.2}Bi_{0.996}SbSe_{0.004}$/Nb/Ni were fabricated by sequentially loading a Ni foil (thickness of 0.1 mm, Hebei Zhanmo Metal Materials Ltd, 99.9%), a Nb foil (thickness of 0.03 mm, Hebei Zhanmo Metal Materials Ltd, 99.9%), $Mg_{3.2}Bi_{0.996}SbSe_{0.004}$ powders, another Nb foil, and another Ni foil into a graphite die with an inner diameter of 10 mm and then densifying them through a one-step SPS technique. Nb foils work as the diffusion barrier layer, and Ni foils work as the metallization layer. The sintering parameters were the same as those used to sinter the $Mg_{3.2}Bi_{0.996}SbSe_{0.004}$ powder, except that the holding time was increased by three minutes, considering the increased thickness of the sample. p-Type TE joints of Ni/$Ti_{88}Al_{12}$/$Ce_{0.9}Fe_3CoSb_{12}$/$Ti_{88}Al_{12}$/Ni were also fabricated by the one-step SPS technique, where a mixture of Ti and Al powders (thickness of 0.1 mm) was used as the barrier layer. The sintering temperature was 873 K, the pressure was 60 MPa, and the holding time was 8 min. After grinding and polishing, the joints were then cut by wire cutting (STX-202A) into dices with dimensions of 3 × 3 × 6 mm^3 for the n-type and 1.7 × 1.7 × 6 mm^3 for the p-type. Both the hot and cold sides of the TE joints were then soldered onto a double-sided direct bonded copper alumina plate using high-temperature Ag paste (CT2700R7S). The overall size of the module consisting of two couples was 10 × 10 × 9 mm^3 (Fig. S13, ESI†). Glass fibers (GXZ aluminosilicate fiber paper) were then filled between TE legs to reduce heat losses due to convection and radiation. Copper wires were soldered to the cold-side Cu electrodes to measure the current and voltage. Prior to high temperature testing, the module resistance at room temperature was measured to ensure good interface bonding and module integrity. Note that BN coatings were sprayed onto the surfaces at hot side of the TE legs to restrain the surface oxidation and sublimation of Mg before the test. In addition, because Mg can react with water, resulting in degradation of the performance, we avoided their contact with water throughout the material processing and device integration process.

Material and module characterization

The phase composition and crystal structure were characterized by powder XRD (Rigaku D/Max-2550 PC) using Cu-Kα radiation (λ = 1.541 Å) at 40 kV and 30 mA. The microstructure and chemical compositions were analyzed by field emission SEM (FE-SEM, TESCAN/MAIA3, Czech) equipped with an energy dispersive spectrometer. The thermal conductivity (κ) was calculated by $\kappa = D \cdot C_p \cdot \rho$, where D, C_p and ρ are the thermal diffusivity, specific heat and density, respectively. D was measured by a laser flash method using an LFA 457 (Netzsch Instruments, Germany), C_p was obtained from the equation in ref. 57, and ρ was measured by the Archimedes method. σ and α were simultaneously measured using a ZEM-3 (ULVAC-RIKO, Japan). The measurement uncertainties for α, σ, and D were ~5%. The Hall coefficient (R_H) was determined using a Hall measurement system (Lakeshore 8400 Series HMS, USA). The carrier concentration (n_H) and mobility (μ_H) were calculated from $n_H = 1/eR_H$ and $\mu_H = \sigma R_H$, where e is the charge of the electron.

The contact resistivity was measured using a homemade four-probe measurement system as detailed in ref. 56. Consolidated sandwiches, *e.g.* $Mg_{3.2}Bi_{0.996}SbSe_{0.004}$/Nb/$Mg_{3.2}Bi_{0.996}SbSe_{0.004}$, obtained by the same sintering process as described above were cut into rectangular bars with dimensions of 3 × 3 × 4 mm^3 and used for the measurements. At least three different positions on each sample were measured to obtain an average value.

The power generation performance of the TE module was characterized using a commercial measurement system (Fig. S13, ESI†) developed by Shanghai Fuyue Vacuum Technology Ltd. The measurement principle is based on the steady-state method similar to that previously reported.[27] Briefly, a TE module is sandwiched between a resistive heater and a circulating

water-cooled Cu block. The cross-sectional area of the heater and Cu block is 10 × 10 mm^2, which is the same as that of the TE module, thus avoiding heat leakage. The efficiency (η) of a TE module is defined as the ratio between the electric power output (P) and the sum of P and Q_{out},

$$\eta = \frac{P}{P + Q_{out}} \quad (2)$$

where Q_{out} is the released heat flow on the cold side. Here, Q_{out} is obtained from the one-dimensional Fourier's law as follows:

$$Q_{out} = A_{Cu}\kappa_{Cu}\Delta T/L \quad (3)$$

where A_{Cu} and κ_{Cu} are the cross-sectional area and thermal conductivity of the Cu block, respectively. ΔT is the temperature difference measured by the thermocouples (T_1 and T_2 in Fig. S14, ESI†) embedded in the Cu block, and L is their vertical distance. During the test, a graphite paper of 0.1 mm thick, thermal grease (QM850) and a uniaxial pressing force of 250 N were used to improve the thermal conduction. Glass fibers were used to completely surround the TE module to reduce the effects of heat radiation and convection. The measurement was carried out in a chamber filled with argon at a pressure of 200 Pa. A program based on LabView software was used to control the power input to the heater. An external direct current electrical load was connected to the module to generate the voltage–current curves. The efficiency uncertainty is approximately 10% based on our previous analysis.[58] In addition, before being put into use, our measurement system was calibrated by comparison with a commercial Mini-PEM apparatus (Ulvac-Riko, Japan). The measurement results of both instruments on one TE module are comparable (Fig. S18, ESI†).

Finite element simulation

The simulation of TE modules was implemented using 3D finite element analyses through ANSYS-Workbench. A full-parameter model coupling the TE effects (conduction, Joule effect, Thomson effect and Peltier effect) and comprehensively considering temperature-dependent material properties was used for accurate simulation. Details can be found in our previous work.[56]

Author contributions

Y. F. and L. W. conceived the ideas and designed the work. Y. F. carried out the experiments including material preparation and characterization, module fabrication and measurements. Z. H. and M. J. contributed to material preparation and interface design. Y. F., Q. Z., and A. H. performed the simulations. S. W. contributed to analysis of the properties of TE materials. Y. F. and Q. Z. wrote the draft. X. A., H. R., L. W., K. N., and W. J. contributed to the discussion and editing.

Conflicts of interest

Y. F., L. W. and W. J. have filed a provisional patent application on the work described here. The status of the patent application is pending.

Acknowledgements

This work was funded by Natural Science Foundation of China (No. 51871053, 52174343), the Innovation Program of Shanghai Municipal Education Commission (202101070003E00110), Shanghai Committee of Science and Technology (No. 20JC1415200). Q. H. Z. acknowledges the financial support from Alexander von Humboldt Foundation (No. CHN 1210297 HFST-P). The authors thank Dr Binbin Jiang from Southern University of Science and Technology for his support on the Mini-PEM measurements.

References

1 Q. Yan and M. G. Kanatzidis, *Nat. Mater.*, 2022, **21**, 503–513.
2 X. Shi and L. Chen, *Nat. Mater.*, 2016, **15**, 691–692.
3 Y. Pei, X. Shi, A. LaLonde, H. Wang, L. Chen and G. J. Snyder, *Nature*, 2011, **473**, 66–69.
4 B. Qin, D. Wang, X. Liu, Y. Qin, J. F. Dong, J. Luo, J. W. Li, W. Liu, G. Tan, X. Tang, J. F. Li, J. He and L. D. Zhao, *Science*, 2021, **373**, 556–561.
5 K. Biswas, J. He, I. D. Blum, C. I. Wu, T. P. Hogan, D. N. Seidman, V. P. Dravid and M. G. Kanatzidis, *Nature*, 2012, **489**, 414–418.
6 B. Jiang, Y. Yu, J. Cui, X. Liu, L. Xie, J. Liao, Q. Zhang, Y. Huang, S. Ning, B. Jia, B. Zhu, S. Bai, L. Chen, S. J. Pennycook and J. He, *Science*, 2021, **371**, 830–834.
7 J. Mao, G. Chen and Z. Ren, *Nat. Mater.*, 2021, **20**, 454–461.
8 Z. Bu, X. Zhang, Y. Hu, Z. Chen, S. Lin, W. Li and Y. Pei, *Energy Environ. Sci.*, 2021, **14**, 6506–6513.
9 P. Ying, R. He, J. Mao, Q. Zhang, H. Reith, J. Sui, Z. Ren, K. Nielsch and G. Schierning, *Nat. Commun.*, 2021, **12**, 1121.
10 Z. Liu, N. Sato, W. Gao, K. Yubuta, N. Kawamoto, M. Mitome, K. Kurashima, Y. Owada, K. Nagase, C. H. Lee, J. Yi, K. Tsuchiya and T. Mori, *Joule*, 2021, **5**, 1196–1208.
11 X. Zhang, Z. Bu, S. Lin, Z. Chen, W. Li and Y. Pei, *Joule*, 2020, **4**, 986–1003.
12 M. Papapetrou, G. Kosmadakis, A. Cipollina, U. La Commare and G. Micale, *Appl. Therm. Eng.*, 2018, **138**, 207–216.
13 T. Xing, Q. Song, P. Qiu, Q. Zhang, M. Gu, X. Xia, J. Liao, X. Shi and L. Chen, *Energy Environ. Sci.*, 2021, **14**, 995–1003.
14 C. Zhou, Y. K. Lee, Y. Yu, S. Byun, Z. Z. Luo, H. Lee, B. Ge, Y. L. Lee, X. Chen, J. Y. Lee, O. Cojocaru-Mirédin, H. Chang, J. Im, S. P. Cho, M. Wuttig, V. P. Dravid, M. G. Kanatzidis and I. Chung, *Nat. Mater.*, 2021, **20**, 1378–1384.
15 Y. Tang, Z. M. Gibbs, L. A. Agapito, G. Li, H.-S. Kim, M. B. Nardelli, S. Curtarolo and G. J. Snyder, *Nat. Mater.*, 2015, **14**, 1223–1228.
16 H. Liu, X. Shi, F. Xu, L. Zhang, W. Zhang, L. Chen, Q. Li, C. Uher, T. Day and G. J. Snyder, *Nat. Mater.*, 2012, **11**, 422–425.
17 W. G. Zeier, J. Schmitt, G. Hautier, U. Aydemir, Z. M. Gibbs, C. Felser and G. J. Snyder, *Nat. Rev. Mater.*, 2016, **1**, 16032.
18 C. S. R. Matthes, D. F. Woerner, T. J. Hendricks, J. P. Fleurial, K. I. Oxnevad, C. D. Barklay and J. F. Zakrajsek, in *2018 IEEE Aerospace Conference*, IEEE, Big Sky; MT, 2018, pp. 1–9.

19 W. D. Liu, D. Z. Wang, Q. Liu, W. Zhou, Z. Shao and Z. G. Chen, *Adv. Energy Mater.*, 2020, **10**, 2000367.
20 H. Tamaki, H. K. Sato and T. Kanno, *Adv. Mater.*, 2016, **28**, 10182–10187.
21 J. Zhang, L. Song, S. H. Pedersen, H. Yin, L. T. Hung and B. B. Iversen, *Nat. Commun.*, 2017, **8**, 13901.
22 K. Imasato, S. D. Kang and G. J. Snyder, *Energy Environ. Sci.*, 2019, **12**, 965–971.
23 J. Mao, H. Zhu, Z. Ding, Z. Liu, G. A. Gamage, G. Chen and Z. Ren, *Science*, 2019, **365**, 495–498.
24 Y. Pan, M. Yao, X. Hong, Y. Zhu, F. Fan, K. Imasato, Y. He, C. Hess, J. Fink, J. Yang, B. Büchner, C. Fu, G. J. Snyder and C. Felser, *Energy Environ. Sci.*, 2020, **13**, 1717–1724.
25 X. Hu, P. Jood, M. Ohta, M. Kunii, K. Nagase, H. Nishiate, M. G. Kanatzidis and A. Yamamoto, *Energy Environ. Sci.*, 2016, **9**, 517–529.
26 B. Jiang, X. Liu, Q. Wang, J. Cui, B. Jia, Y. Zhu, J. Feng, Y. Qiu, M. Gu, Z. Ge and J. He, *Energy Environ. Sci.*, 2020, **13**, 579–591.
27 Q. Zhang, Z. Zhou, M. Dylla, M. T. Agne, Y. Pei, L. Wang, Y. Tang, J. Liao, J. Li and S. Bai, *Nano Energy*, 2017, **41**, 501–510.
28 G. Nie, W. Li, J. Guo, A. Yamamoto, K. Kimura, X. Zhang, E. B. Isaacs, V. Dravid, C. Wolverton, M. G. Kanatzidis and S. Priya, *Nano Energy*, 2019, **66**, 104193.
29 J. Chu, J. Huang, R. Liu, J. Liao, X. Xia, Q. Zhang, C. Wang, M. Gu, S. Bai, X. Shi and L. Chen, *Nat. Commun.*, 2020, **11**, 2723.
30 I. Aoyama, H. Kaibe, L. Rauscher, T. Kanda, M. Mukoujima, S. Sano and T. Tsuji, *Jpn. J. Appl. Phys.*, 2005, **44**, 4275.
31 K. Bartholomé, B. Balke, D. Zuckermann, M. Köhne, M. Müller, K. Tarantik and J. König, *J. Electron. Mater.*, 2014, **43**, 1775–1781.
32 J. Yu, Y. Xing, C. Hu, Z. Huang, Q. Qiu, C. Wang, K. Xia, Z. Wang, S. Bai, X. Zhao, L. Chen and T. Zhu, *Adv. Energy Mater.*, 2020, **10**, 2000888.
33 Y. Xing, R. Liu, J. Liao, C. Wang, Q. Zhang, Q. Song, X. Xia, T. Zhu, S. Bai and L. Chen, *Joule*, 2020, **4**, 2475–2483.
34 P. Qiu, T. Mao, Z. Huang, X. Xia, J. Liao, M. T. Agne, M. Gu, Q. Zhang, D. Ren, S. Bai, X. Shi, G. J. Snyder and L. Chen, *Joule*, 2019, **3**, 1538–1548.
35 P. Jood, M. Ohta, A. Yamamoto and M. G. Kanatzidis, *Joule*, 2018, **2**, 1339–1355.
36 C. Fu, S. Bai, Y. Liu, Y. Tang, L. Chen, X. Zhao and T. Zhu, *Nat. Commun.*, 2015, **6**, 8144.
37 #ChemistryAdvent #IYPT2019 Day 23, **https://www.compoundchem.com/2019advent/day23/**, (accessed January 6, 2022).
38 J. Zhang, L. Song, A. Mamakhel, M. R. V. Jørgensen and B. B. Iversen, *Chem. Mater.*, 2017, **29**, 5371–5383.
39 F. Zhang, C. Chen, H. Yao, F. Bai, L. Yin, X. Li, S. Li, W. Xue, Y. Wang, F. Cao, X. Liu, J. Sui and Q. Zhang, *Adv. Funct. Mater.*, 2020, **30**, 1906143.
40 J. Liang, H. Yang, C. Liu, L. Miao, J. Chen, S. Zhu, Z. Xie, W. Xu, X. Wang, J. Wang, B. Peng and K. Koumoto, *ACS Appl. Mater. Interfaces*, 2020, **12**, 21799–21807.
41 X. Mo, J. Liao, G. Yuan, S. Zhu, X. Lei, L. Huang, Q. Zhang, C. Wang and Z. Ren, *J. Magnesium Alloys*, 2022, **10**, 1024–1032.
42 T. Kanno, H. Tamaki, H. K. Sato, S. D. Kang, S. Ohno, K. Imasato, J. J. Kuo, G. J. Snyder and Y. Miyazaki, *Appl. Phys. Lett.*, 2018, **112**, 033903.
43 J. J. Kuo, S. D. Kang, K. Imasato, H. Tamaki, S. Ohno, T. Kanno and G. J. Snyder, *Energy Environ. Sci.*, 2018, **11**, 429–434.
44 L. Yin, C. Chen, F. Zhang, X. Li, F. Bai, Z. Zhang, X. Wang, J. Mao, F. Cao, X. Chen, J. Sui, X. Liu and Q. Zhang, *Acta Mater.*, 2020, **198**, 25–34.
45 J. Yang, G. Li, H. Zhu, N. Chen, T. Lu, J. Gao, L. Guo, J. Xiang, P. Sun, Y. Yao, R. Yang and H. Zhao, *Joule*, 2021, S2542435121005341.
46 L. Yin, *Master thesis*, School of Materials Science and Engineering, and Institute of Materials Genome & Big Data, Harbin Institute of Technology, 2019, **https://cdmd.cnki.com.cn/Article/CDMD-10213-1019690487.htm** (accessed in June 2022).
47 Q. H. Zhang, X. Y. Huang, S. Q. Bai, X. Shi, C. Uher and L. D. Chen, *Adv. Eng. Mater.*, 2016, **18**, 194–213.
48 W. Liu and S. Bai, *J. Materiomics*, 2019, **5**, 321–336.
49 J. Sui, J. Li, J. He, Y. L. Pei, D. Berardan, H. Wu, N. Dragoe, W. Cai and L. D. Zhao, *Energy Environ. Sci.*, 2013, **6**, 2916.
50 J. Lin, X. Li, G. Qiao, Z. Wang, J. Carrete, Y. Ren, L. Ma, Y. Fei, B. Yang, L. Lei and J. Li, *J. Am. Chem. Soc.*, 2014, **136**, 1497–1504.
51 Y. He, T. Day, T. Zhang, H. Liu, X. Shi, L. Chen and G. J. Snyder, *Adv. Mater.*, 2014, **26**, 3974–3978.
52 K. Zhao, A. B. Blichfeld, H. Chen, Q. Song, T. Zhang, C. Zhu, D. Ren, R. Hanus, P. Qiu, B. B. Iversen, F. Xu, G. J. Snyder, X. Shi and L. Chen, *Chem. Mater.*, 2017, **29**, 6367–6377.
53 Z. Ren, J. Shuai, J. Mao, Q. Zhu, S. Song, Y. Ni and S. Chen, *Acta Mater.*, 2018, **143**, 265–271.
54 H. Zhu, R. He, J. Mao, Q. Zhu, C. Li, J. Sun, W. Ren, Y. Wang, Z. Liu, Z. Tang, A. Sotnikov, Z. Wang, D. Broido, D. J. Singh, G. Chen, K. Nielsch and Z. Ren, *Nat. Commun.*, 2018, **9**, 2497.
55 J. Shuai, H. Geng, Y. Lan, Z. Zhu, C. Wang, Z. Liu, J. Bao, C.-W. Chu, J. Sui and Z. Ren, *Proc. Natl. Acad. Sci. U. S. A.*, 2016, **113**, E4125–E4132.
56 Q. Zhang, J. Liao, Y. Tang, M. Gu, C. Ming, P. Qiu, S. Bai, X. Shi, C. Uher and L. Chen, *Energy Environ. Sci.*, 2017, **10**, 956–963.
57 M. T. Agne, K. Imasato, S. Anand, K. Lee, S. K. Bux, A. Zevalkink, A. J. E. Rettie, D. Y. Chung, M. G. Kanatzidis and G. J. Snyder, *Mater. Today Phys.*, 2018, **6**, 83–88.
58 X. Lu, Q. Zhang, J. Liao, H. Chen, Y. Fan, J. Xing, S. Gu, J. Huang, J. Ma and J. Wang, *Adv. Energy Mater.*, 2020, **10**, 1902986.

